REPORTS

VOLCANOLOGY

The Yellowstone magmatic system from the mantle plume to the upper crust

Hsin-Hua Huang,[1,2]* Fan-Chi Lin,[1] Brandon Schmandt,[3] Jamie Farrell,[1] Robert B. Smith,[1] Victor C. Tsai[2]

The Yellowstone supervolcano is one of the largest active continental silicic volcanic fields in the world. An understanding of its properties is key to enhancing our knowledge of volcanic mechanisms and corresponding risk. Using a joint local and teleseismic earthquake *P*-wave seismic inversion, we revealed a basaltic lower-crustal magma body that provides a magmatic link between the Yellowstone mantle plume and the previously imaged upper-crustal magma reservoir. This lower-crustal magma body has a volume of 46,000 cubic kilometers, ~4.5 times that of the upper-crustal magma reservoir, and contains a melt fraction of ~2%. These estimates are critical to understanding the evolution of bimodal basaltic-rhyolitic volcanism, explaining the magnitude of CO_2 discharge, and constraining dynamic models of the magmatic system for volcanic hazard assessment.

The interaction of the North American Plate moving southwestward across a mantle plume created the Snake River Plain, a bimodal basalt-rhyolite volcanic system dating to 16.5 million years ago (Ma) (*1*). The Yellowstone volcanic field that sits at the eastern end of the plain is the youngest manifestation of the hotspot and is characterized by extensive earthquakes (*2*, *3*), episodic ground deformation (*4*), high heat flux averaging 2000 mW m^{-2} (*2*, *5*), and the largest continental hydrothermal system in the world (*6*, *7*). The most recent cataclysmic eruption occurred at 0.64 Ma and created the 40 km × 60 km Yellowstone caldera, which is filled with rhyolitic lava flows as young as 70,000 years (Fig. 1). Earlier teleseismic studies have imaged a west-northwest–dipping plume extending into the top of the lower mantle (*8*–*11*). Local earthquake tomography and waveform modeling studies have revealed an upper-crustal magma reservoir between 5 and 16 km depth (*3*, *12*, *13*), of which the shallowest portion correlates with the largest area of hydrothermal activity and extends 15 km northeast of the caldera (*3*). Even with a large volume of >4000 km^3 and a high melt fraction of up to 32% (*2*, *3*, *13*), this upper-crustal reservoir cannot account for the large CO_2 flux of 4.5×10^7 kg daily and requires additional input of basaltic magma invading the lower to middle crust (*6*, *7*). Moreover, it is unclear how the mantle plume interacts with the crustal volcanic system. The connection between the shallow magma reservoir (above 16 km depth) and the deep mantle plume (below 60 km depth) is therefore a critical component to understand the entire Yellowstone magmatic system but has never been imaged distinctly, despite other geophysical and geologic

[1]Department of Geology and Geophysics, University of Utah, Salt Lake City, UT 84112, USA. [2]Seismological Laboratory, California Institute of Technology, Pasadena, CA 91125, USA. [3]Department of Earth and Planetary Sciences, University of New Mexico, Albuquerque, NM 87131, USA.
*Corresponding author. E-mail: hsinhua.huang@utah.edu

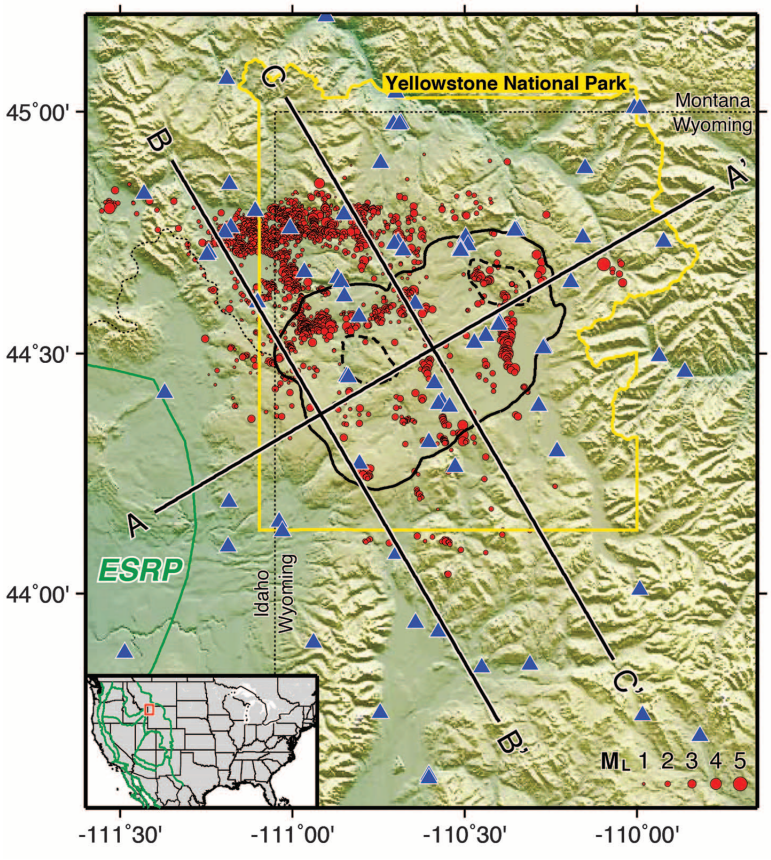

Fig. 1. Map of the seismic stations used in this study and the *P*-wave velocity cross-section locations in the Yellowstone area. Stations and earthquakes are denoted by blue triangles and red dots, respectively. Black solid and dashed lines outline the Late Quaternary Yellowstone caldera and resurgent domes. Green lines represent the tectonic division of the Eastern Snake River Plain (ESRP). Yellow and thin dotted lines are the border of Yellowstone National Park and the surrounding state borders, respectively. Locations of the cross sections in Fig. 3 are shown by thick black lines with labels. The inset map shows the location of the Yellowstone area (red box) and the major tectonic boundaries (green lines) in the western United States.

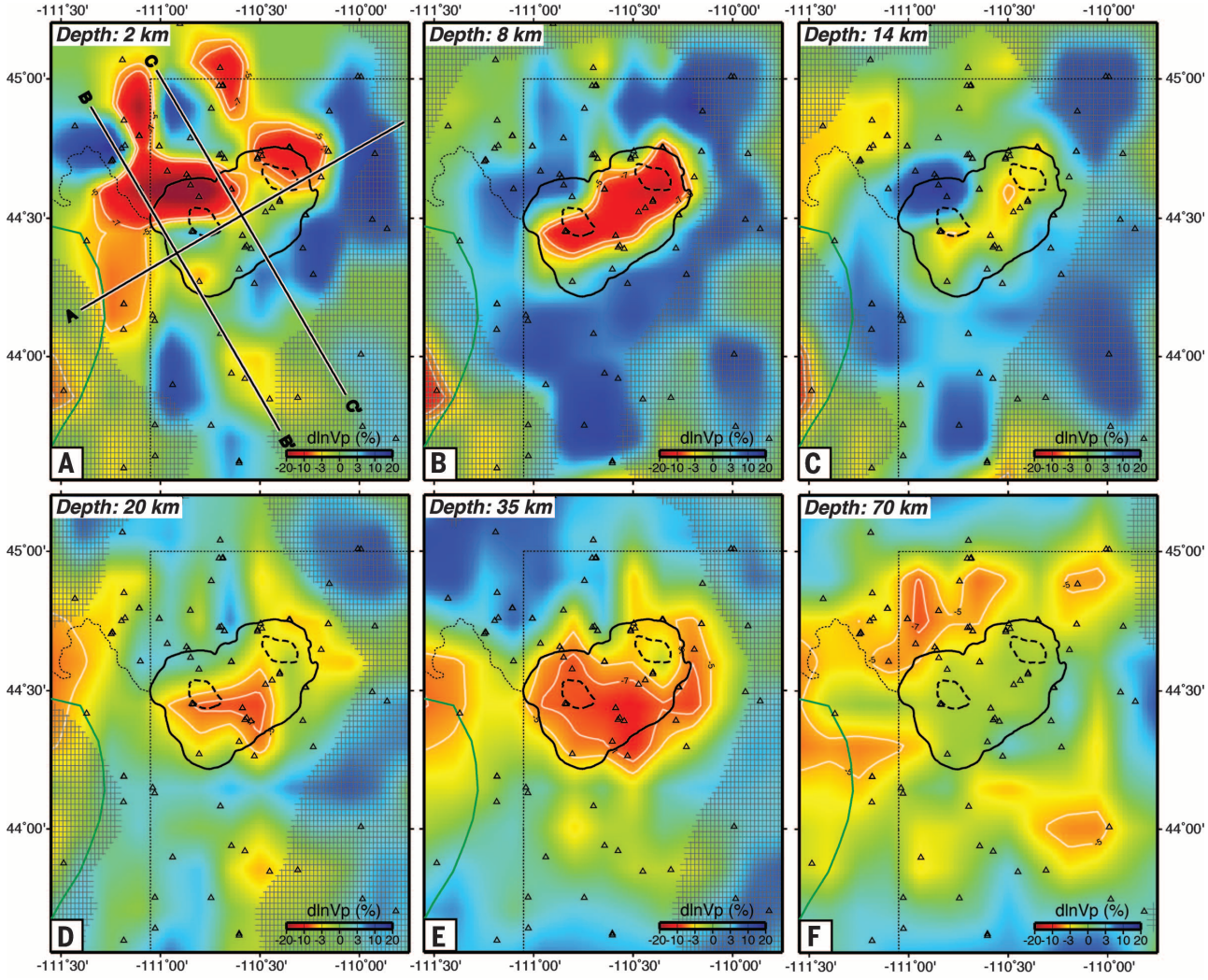

Fig. 2. Depth slices of the Yellowstone tomographic *P*-wave model. (**A** to **E**) Crustal velocity structures; (**F**) upper-mantle velocity structure. Black solid and dashed lines outline the 0.64 Ma caldera and resurgent domes. The green line is the northeast end of the Eastern Snake River Plain. White lines denote the 5% and 7% *P*-wave velocity reduction contours. Poorly resolved areas are shaded according to the index of resolvability, *R*, converted from the checkerboard test results (*25*).

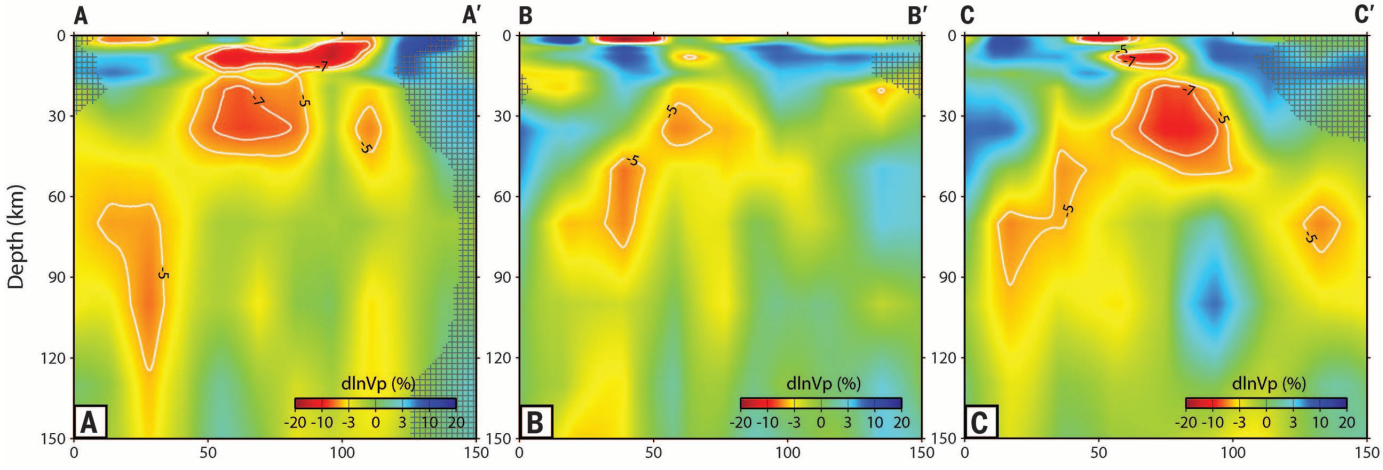

Fig. 3. Cross sections of the Yellowstone tomographic *P*-wave model. (**A** to **C**) The crustal magmatic reservoirs and the mantle plume are demonstrated in northeast-southwest (A) and northwest-southeast [(B) and (C)] directions, respectively. Map-view locations of the cross sections are shown in Fig. 1. White lines denote the 5% and 7% *P*-wave velocity reduction contours. Poorly resolved areas are shaded according to the index of resolvability, *R*, converted from the checkerboard test results (*25*).

evidence that hypothesizes the presence of a continuous crustal magma body (*2*, *5*, *7*).

Imaging the position and size of the entire volcanic plumbing system is also important to constrain magmatic dynamics modeling for further hazard assessment (*14*). Many local seismic array experiments have been conducted on volcanoes such as Askja, Iceland (*15*); Axial, Juan de Fuca mid-ocean ridge (*16*); Kilauea, Hawaii (*17*); and Mount St. Helens, Washington (*18*). A common observation of these experiments is an imaged shallow low-velocity body (LVB) at depths of 5 to 10 km, which is often interpreted as a magma reservoir. Several of these studies also image the top of a second LVB at greater crustal depths (*18*, *19*); however, they usually quickly lose resolution with depth because of the limited array aperture and the shallowly distributed earthquakes (often less than ~10 km depth). Large arrays for teleseismic tomography can only focus on mantle images and poorly resolved crustal structures. A complete framework of the mantle-crust volcanic system under volcanoes has not yet been elucidated.

By combining data from the dense seismic arrays of the Yellowstone, Teton, and Snake River Plain (SRP) regional seismic networks, the NOISY array (*20*), and the wide-aperture EarthScope Transportable Array (Fig. 1), we present an image of the entire volcanic plumbing system beneath the Yellowstone caldera and reveal a large basaltic magma reservoir in the lower to middle crust by using a joint tomographic inversion of local and teleseismic earthquake data (*21*–*23*). The seismic data used in this study were compiled from previous studies (*3*, *24*) and consist of 47,815 *P*-wave first arrivals from 4520 local earthquakes and 4605 relative arrival times from 329 teleseismic earthquakes. A local earthquake inversion is first conducted to obtain a three-dimensional initial crustal model and reduce the dominance of the local data prior to the joint inversion (*25*).

We found a large east-northeast–west-southwest elongated LVB beneath the Yellowstone caldera (Fig. 2, A to C, and Fig. 3A) at depths shallower than 20 km, consistent with previous studies (*3*, *25*). However, at depths of 20 to 50 km, another larger LVB with >5% *P*-wave velocity (V_P) reduction also emerges in our model (Fig. 2, D and E, and Fig. 3, A and C). From cross section AA´ (Fig. 1 and Fig. 3A), it is clear that this deeper LVB is immediately beneath the shallow LVB. The existence of the lower-crustal LVB and the separation between the two imaged crustal LVBs are validated through characteristic-model synthetic tests and finite-frequency analysis (*25*), indicating that the deep crustal LVB is a separate magma reservoir in the middle to lower crust, based on a Moho depth of ~45 km in this area (*26*). The LVB separates into two zones northwest and southeast of the caldera at mantle depths of ~70 km (Fig. 2F). The orientation of the northwestern portion agrees with the extension of the SRP in a northeast-southwest direction, implying the track of the North American Plate across the Yellowstone plume (*2*, *10*). In cross sections BB´ and CC´, this low-velocity zone that dips ~60° northwestward is consistent with the plume geometry determined in previous studies (*8*–*10*). In contrast, the southeastern low-velocity zone is relatively smaller and localized, terminating at a depth of 100 km (Fig. 3C).

The V_P reduction of >5% within the imaged crustal LVBs is difficult to explain by temperature and composition alone and implies the presence of melts (*25*). We assume a 5% V_P reduction as being diagnostic of partial melt (*3*) to quantitatively estimate the volume of crustal melt. Weaker anomalies may also be partly explained by partial melt, but tradeoffs with temperature or composition variations and tomographic resolution prevent these weaker anomalies from being robustly interpreted as melt. Using this conservative proposition results in volume estimates of ~46,000 km^3 for the lower-crustal LVB and ~10,000 km^3 for the upper-crustal LVB. These estimates agree well with the sizes and depths of the basaltic and rhyolitic magma reservoirs interpreted by geochemical studies (*6*, *7*, *27*). The melt fraction of the upper-crustal LVB has been previously estimated to range from 5 to 32% (*2*, *3*, *13*). With an average V_P of 5.21 km/s calculated over the volume of the upper-crustal LVB, we estimate a melt fraction of ~9% (*25*), based on a velocity-melt fraction relation derived for the Yellowstone granite-rhyolite-melt system (*13*). For the lower-crustal LVB, we assume similar elastic properties between the lower crust and the uppermost mantle and use previously proposed partial derivatives of V_P with respect to melt fraction for a peridotite-basalt-melt system (table S2). Given the calculated average V_P reduction of 6.56%, a ~2% fraction of basaltic partial melts is preferred (*25*). Multiplying the melt fraction of each LVB by its volume gives ~900 km^3 of rhyolitic melts and also ~900 km^3 of basaltic partial melts. These estimates provide an overall volume estimate that is comparable to the explosive material volumes of the last three Yellowstone giant eruptions at 2.1 Ma (2500 km^3), 1.3 Ma (280 km^3), and 0.64 Ma (1000 km^3) (*1*). Although lower-crustal basaltic melts are not expected to contribute to the caldera-forming eruptions, and the upper-crustal melts are unlikely to erupt at one time, both melt volumes can feed smaller eruptions. Assuming a CO_2 degassing rate of 4.5×10^7 kg per day, 50% of which comes from subsurface magma discharge (*28*), the addition of a basaltic lower-crustal reservoir can provide a sufficient influx (*25*) for the reported ~15,000-year history of the intensive hydrothermal degassing system (*29*).

Our seismic images depict characteristics of the entire Yellowstone magmatic system from the upper mantle to the crust (Fig. 4) in which the west-northwest–dipping plume is the magmatic source that generates the mafic/basaltic partial melts that intrude into the lower crust, fractionate, and melt the crust to produce more silicic magma, and then intermittently ascend to shallower depths to form the dominantly rhyolitic reservoir at depths of 4 to 14 km beneath the Yellowstone caldera. Because volcanic sills act as traps that accumulate upward-migrating magmatic fluids to form a magma reservoir (*2*, *3*, *6*, *30*–*32*), the two large LVBs observed in our model suggest the presence of two sill complexes in the upper and lower crust that are likely linked by dikes. This layered structure of basaltic intrusions was also suggested for the volcanic crustal structure in the nearby eastern Snake River Plain (*33*). This model may thus be representative of other bimodal basaltic-rhyolitic volcanoes around the

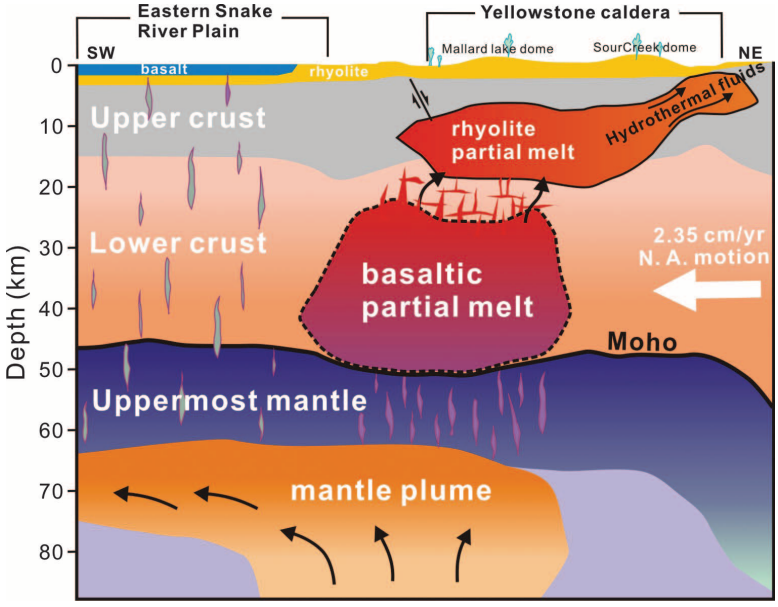

Fig. 4. Schematic model for the Yellowstone crust–upper mantle magmatic system. The orientation of the model is along the cross section AA´ in Fig. 3. The geometry of the upper- and lower-crustal magma reservoirs is based on the contour of 5% V_P reduction in the tomographic model. The dashed outline of the lower-crustal magma reservoir indicates the larger uncertainties in its boundaries relative to that of the upper reservoir (*25*). The white arrow indicates the North American plate motion of 2.35 cm/year.

world. The estimates of volume and geometry of crustal magma reservoirs may also be critical for realistic modeling magmatic system dynamics (*14*) that in turn could provide further information for volcanic hazard models.

REFERENCES AND NOTES

1. R. L. Christiansen, *U.S. Geol. Surv. Prof. Pap. 729-G*, 145 (2001).
2. R. B. Smith *et al.*, *J. Volcanol. Geotherm. Res.* **188**, 26–56 (2009).
3. J. Farrell, R. B. Smith, S. Husen, T. Diehl, *Geophys. Res. Lett.* **41**, 3068–3073 (2014).
4. W. L. Chang, R. B. Smith, C. Wicks, J. M. Farrell, C. M. Puskas, *Science* **318**, 952–956 (2007).
5. K. R. DeNosaquo, R. B. Smith, A. R. Lowry, *J. Volcanol. Geotherm. Res.* **188**, 108–127 (2009).
6. J. B. Lowenstern, S. Hurwitz, *Elements* **4**, 35–40 (2008).
7. S. Hurwitz, J. B. Lowenstern, *Rev. Geophys.* **52**, 375–411 (2014).
8. H. Yuan, K. Dueker, *Geophys. Res. Lett.* **32**, L07304 (2005).
9. M. Xue, R. M. Allen, *J. Geophys. Res.* **115**, B07303 (2010).
10. M. Obrebski, R. M. Allen, F. Pollitz, S. H. Hung, *Geophys. J. Int.* **185**, 1003–1021 (2011).
11. B. Schmandt, K. Dueker, E. Humphreys, S. Hansen, *Earth Planet. Sci. Lett.* **331–332**, 224–236 (2012).
12. S. Husen, R. B. Smith, G. P. Waite, *J. Volcanol. Geotherm. Res.* **131**, 397–410 (2004).
13. R. Chu, D. V. Helmberger, D. Sun, J. M. Jackson, L. Zhu, *Geophys. Res. Lett.* **37**, L01306 (2010).
14. M. Paulatto *et al.*, *Geochem. Geophys. Geosyst.* **13**, Q01014 (2012).
15. M. A. Mitchell, R. S. White, S. Roecker, T. Greenfield, *Geophys. Res. Lett.* **40**, 5040–5046 (2013).
16. M. West, W. Menke, M. Tolstoy, S. Webb, R. Sohn, *Nature* **413**, 833–836 (2001).
17. E. M. Syracuse *et al.*, *J. Geophys. Res.* **115**, B10310 (2010).
18. G. P. Waite, S. C. Moran, *J. Volcanol. Geotherm. Res.* **182**, 113–122 (2009).
19. I. Koulakov *et al.*, *J. Volcanol. Geotherm. Res.* **263**, 75–91 (2013).
20. K. J. Seats, J. F. Lawrence, *Geophys. Res. Lett.* **41**, 8277–8282 (2014).
21. S. W. Roecker *et al.*, *J. Geophys. Res.* **98**, 15779 (1993).
22. D. Zhao, A. Hasegawa, H. Kanamori, *J. Geophys. Res.* **99**, 22313–22329 (1994).
23. H.-H. Huang *et al.*, *Geophys. Res. Lett.* **41**, 10.1002/2014GL061115 (2014).
24. B. Schmandt, F. C. Lin, *Geophys. Res. Lett.* **41**, 6342–6349 (2014).
25. See supplementary materials on *Science* Online.
26. W. Shen, M. H. Ritzwoller, V. Schulte-Pelkum, *J. Geophys. Res.* **118**, 262–276 (2013).
27. S. M. White, J. A. Crisp, F. J. Spera, *Geochem. Geophys. Geosyst.* **7**, Q03010 (2006).
28. C. Werner, S. Brantley, *Geochem. Geophys. Geosyst.* **4**, 1061 (2003).
29. R. O. Fournier, *Annu. Rev. Earth Planet. Sci.* **17**, 13–53 (1989).
30. K. Jaxybulatov *et al.*, *Science* **346**, 617–619 (2014).
31. C. Annen, J. D. Blundy, R. S. J. Sparks, *J. Petrol.* **47**, 505–539 (2006).
32. A. Gudmundsson, *Tectonophysics* **500**, 50–64 (2011).
33. J. W. Shervais, S. K. Vetter, B. B. Hanan, *Geology* **34**, 365 (2006).

ACKNOWLEDGMENTS

Data were collected from the Yellowstone seismograph network operated by the University of Utah, the NSF-funded EarthScope project, and a temporary seismic array operated by Stanford University. All waveform data used in this project can be obtained through the IRIS Data Management Center. Supported by the University of Utah, the University of Utah Seismograph Stations, NSF grants CyberSEES-1442665, EAR-1252191, and EAR-03233309 (in support of the EarthScope Transportable Array), and the Brinson Foundation and Carrico funds.

SUPPLEMENTARY MATERIALS

www.sciencemag.org/content/348/6236/773/suppl/DC1
Materials and Methods
Figs. S1 to S7
Tables S1 to S3
References (*34–48*)

20 January 2015; accepted 1 April 2015
Published online 23 April 2015;
10.1126/science.aaa5648

QUANTUM OPTICS

Quantum dynamics of an electromagnetic mode that cannot contain *N* photons

L. Bretheau, P. Campagne-Ibarcq, E. Flurin, F. Mallet, B. Huard*

Electromagnetic modes are instrumental in building quantum machines. In this experiment, we introduce a method to manipulate these modes by effectively controlling their phase space. Preventing access to a single energy level, corresponding to a number of photons *N*, confined the dynamics of the field to levels 0 to *N* – 1. Under a resonant drive, the level occupation was found to oscillate in time, similarly to an *N*-level system. Performing a direct Wigner tomography of the field revealed its nonclassical features, including a Schrödinger cat–like state at half period in the evolution. This fine control of the field in its phase space may enable applications in quantum information and metrology.

The manipulation of a quantum system usually involves the control of its Hamiltonian in time. An alternative route consists in effectively tailoring its Hilbert space dynamically. This can be done by restricting the system evolution to a subset of possible states. When even a single energy level is disabled, the system evolution is deeply modified and is ruled by the so-called quantum Zeno dynamics (QZD) (*1–5*). As the name suggests, the level blockade can be realized by repeatedly checking whether the level is occupied, owing to the inherent back action of quantum measurements (*1*, *2*, *6*). Alternatively, as in the present experiment, QZD can be achieved by blocking the level using a strong, active coupling to an ancillary quantum system (*3–5*), without any measurement (*7*). These ideas have recently been demonstrated for atoms, using either Rb Bose-Einstein condensates (*8*) or Rydberg atoms (*9*). However, the dynamics of these systems are intrinsically confined to a finite number of energy levels. Here, using a circuit quantum electrodynamics architecture, we implement QZD of light. With its large number of energy levels and ease of control, a single electromagnetic mode offers a wider and more controllable phase space than atoms and two-level systems.

The principle of our experiment is shown in Fig. 1. One cavity mode of frequency f_c is coupled to a qubit of frequency f_q. For a large enough detuning, their evolution can be described by the dispersive Hamiltonian $hf_c a^\dagger a + hf_q|e\rangle\langle e| - h\chi a^\dagger a|e\rangle\langle e|$, where h is Planck's constant, $a^\dagger$ is the ladder operator, and $|e\rangle$ is the excited state of the qubit. The last term describes the frequency shift of the cavity (qubit) $-\chi$, which occurs when the qubit (cavity) is excited by one extra quantum of energy. Owing to this shift, a tone at frequency $f_q - N\chi$ addresses only the transition between states $|N\rangle \otimes |g\rangle$ and $|N\rangle \otimes |e\rangle$ for level widths smaller than χ (*10*); here, $|g\rangle$ is the ground state of the qubit. These levels then hybridize and repel each other. Their splitting is given by the Rabi frequency Ω_R, at which the qubit population would oscillate in the case where the cavity is in state $|N\rangle$ (Fig. 1). Any transition to level N is now forbidden when the cavity is driven at resonance. Schematically, level N has been moved out of the harmonic ladder (Fig. 1). Then, starting from the ground state, the electromagnetic mode is confined to levels 0 to $N-1$, whereas the qubit remains in its ground state. The field dynamics is dramatically changed, resembling that of an N-level system, and nonclassical states similar to "Schrödinger cat states" develop.

In the experiment, we use the fundamental mode of a three-dimensional (3D) microwave cavity made out of bulk aluminum, which resonates at $f_c = 7.804$ GHz. This mode is off-resonantly coupled to a superconducting qubit (*11*) with bare frequency $f_q = 5.622$ GHz and dispersive frequency shift $\chi = 4.63$ MHz. The cavity exit rate $\gamma_c = (1.3\ \mu s)^{-1}$ is dominated by the coupling rate to two transmission lines connected to the cavity, which are used for both driving and the readout of the system. The relaxation rate $\gamma_1 = (11.5\ \mu s)^{-1}$ and decoherence rate $\gamma_2 = (8.9\ \mu s)^{-1}$ of the ancillary qubit are an order of magnitude smaller.

The experiment is performed by first turning on the blocking tone at $f_q - N\chi$. For the level blockade to be effective, we choose $\Omega_R = 6.24$ MHz, much larger than the level frequency width, which is about γ_c. Then, the cavity is driven at frequency $f_d \approx f_c$ for a time t varying up to a few μs. The drive power is fixed throughout the experiment and would lead to an amplitude displacement rate ε_d of about $3\ \mu s^{-1}$ in the cavity, were there neither damping nor nonlinearities. At time t, both the blocking signal and the cavity drive are turned off, and the field state is measured. Two measurement schemes are used to characterize the cavity state. Both methods use as a probe the same qubit that is used to provide the level blockade.

The first method consists in measuring the probability P_k for the field to host k photons. To do so, a selective π pulse is applied to the qubit at frequency $f_q - k\chi$ so that it gets excited if k photons are in the cavity. Measuring

Laboratoire Pierre Aigrain, Ecole Normale Supérieure–PSL Research University, CNRS, Université Pierre et Marie Curie–Sorbonne Universités, Université Paris Diderot–Sorbonne Paris Cité, 24 Rue Lhomond, 75231 Paris Cedex 05, France.
***Corresponding author. E-mail: benjamin.huard@ens.fr**

www.sciencemag.org/cgi/content/full/science.aaa5648/DC1

Supplementary Materials for

The Yellowstone magmatic system from the mantle plume to the upper crust

Hsin-Hua Huang,* Fan-Chi Lin, Brandon Schmandt, Jamie Farrell, Robert B. Smith, Victor C. Tsai

*Corresponding author. E-mail: hsinhua.huang@utah.edu

Published 23 April 2015 on *Science* Express
DOI: 10.1126/science.aaa5648

This PDF file includes:

Materials and Methods

Seismic tomographic methods and model parameterization

A recently developed code for multi-dataset tomographic joint inversion is employed in this study (*23, 34-36*), in which the absolute travel-time residuals from local earthquake data and the relative travel-time residuals from teleseismic data are simultaneously minimized. For the travel-time calculation, we used the modified pseudobending method in three-dimensional (3-D) spherical coordinates (*37, 38*), and retraced the local and teleseismic rays after each iteration with a nonlinear approximation. The 3-D velocity model is parameterized with a spatial grid of 15 km in longitude and latitude and incremental depth nodes from -10 to 160 km as shown in Table S1. The initial 1-D *P*-wave velocity (V_P) model follows the ak135 global 1-D model (*39*) but employs a local 1-D model (*3*) for the shallowest 20-km depth (Table S1).

Since the number of local earthquake absolute *P*-wave arrival times is 10 times more than the teleseismic differential arrival time dataset, these two datasets should not be weighted equally. However, in this study we weighted both types of data equally but decoupled their mutual influence with a two-step approach (*23*). We inverted the local earthquake data for a 3-D *P*-wave crustal model first, and then used the resulting 3-D model as an initial model for the joint inversion of both local and teleseismic data in the second step. In this way, the residuals of local seismic data have been reduced as much as possible in the first inversion and do not dominate the following joint inversion. After 8 iterations (4 with local earthquake data alone and 4 with joint inversion), the total residual RMS decreases from 0.282 to 0.134 s, a 52% reduction. Fig. S1 shows that all station residuals are reduced significantly after the two-step inversion. By extensively testing the regularization parameters, a damping factor of 40 and a smoothing factor of 30 were chosen for the final analyses (Fig. S2).

Because the Yellowstone local earthquake data set (*3*) is used in this study, the upper-crustal low velocity body (LVB) in our model is very similar to that of (*3*) in geometry but is greater in size and anomaly magnitude. The greater size and magnitude may mainly arise from differences in coordinates and ray tracing methods between our code and the open-source program *simulps14* used in (*3*). The spherical coordinates we used tend to trace shorter paths than the flattened Cartesian coordinates do, and in turn require slower low velocity anomalies to compensate for the shorter/faster path. The coordinate effect would be more significant for the teleseismic data on a scale of over 200 km (*40*). In this sense, rather than using the existing local model of (*3*), it is also better to re-invert the local earthquake data in spherical coordinates to achieve consistency with the teleseismic data.

Resolution tests with checkerboard and characteristic models

We conducted conventional seismic tomography checkerboard tests and characteristic-model synthetic tests for resolution assessment. In the checkerboard test, we input a checkerboard-like model with -5% and 5% variations in *P*-wave velocity (V_P), interchanging two nodes at a time horizontally and three nodes at a time vertically except for the top two nodes. Results show generally good recovery at each depth slice (Fig. S3). Velocity variations between 8 and 14 km, 35 and 50 km, and 100 and 130 km are resolved relatively poorer compared to other depths because the velocities there vary sharply in three dimensions rather than primarily laterally as in the other depth slices.

A characteristic model was designed according to the model images we obtained in Fig. 3, with four prominent low velocity anomalies (LVA). The LVAs at 4-14 and 20-40 km represent the upper and lower magma reservoirs, and the other two deep LVAs represent the plume-like feature and localized mantle velocity anomaly to the northwest and southeast of the caldera (Fig. S4). Performing inversions using local data alone, teleseismic data alone, and with both types of data, the results clearly demonstrate the capability of the joint inversion to resolve the entire crustal magmatic system. The results also show the robust nature of the separation between the two LVAs in the crust. However, because of a smearing effect caused by the similar incident angles of sub-vertical teleseismic incoming rays, the bottom of the lower-crustal LVA is smeared downward to connect with the plume anomaly, as we saw in the real data inversion (Fig. 3C). This similarity implies that the bottom of the lower crustal reservoir is possibly shallower than imaged in our model. Thus, this reservoir likely lies within the crust, i.e., above ~45 km in the Yellowstone area (*26*) as shown in Fig. 4. The results of another negative test of a characteristic model without the lower-crustal LVA are also displayed in Fig. S5, confirming that the existence of a lower-crustal LVA is resolvable and robust although a slight smearing anomaly in the lower crust is present.

To further test how noise in the data causes smearing, we introduced random noise centered at 0 s with a standard deviation of 0.13 s (based on the RMS travel time residuals of the final real-data inversion) into the synthetic travel times (Fig. S6). The results show that the smearing at the bottom of the lower-crustal LVB and some streaking artifacts are enhanced (indicated by black arrows); however, the main features we interpret clearly remain and are not likely due to data noise.

Resolvability index translation

Based on the results of the checkerboard test, we translated the model recovery level into a resolvability index, *R* (*36*, *41*), which is defined as

$$R = \frac{\sum_{i=i-n}^{i+n}\sum_{j=j-n}^{j+n}\sum_{k=k-n}^{k+n}\left(Vt_{i,j,k}+Vr_{i,j,k}\right)^2}{2\sum_{i=i-n}^{i+n}\sum_{j=j-n}^{j+n}\sum_{k=k-n}^{k+n}\left(Vt_{i,j,k}^2+Vr_{i,j,k}^2\right)} \quad \text{(S1)}$$

where *Vt* are the true velocities (i.e., from a known synthetic model) and *Vr* are the recovered velocities at nodes denoted by indices *i, j, k* in 3-D space. This resolvability factor is then operated over a defined range by a desired number of nodes, *n*. A larger value of *n* produces a smoother map and vice versa. We chose $n = 5$ in this case, which is slightly larger than the perturbation wavelength ($n = 3$) in the checkerboard test and generally produces good results. *R* ranges from 0 to 1, in which $R = 1$ represents the velocity anomaly is 100% recovered (nodes with significant ray crossing), $R = 0.5$ indicates 0% recovered (nodes with no rays crossing), and $R = 0$ denotes a velocity that is −100% perturbed (unstable inversion nodes). The corresponding *R* index and the derivative weighted sum (DWS) (*42*) map at different depths are also shown in Fig. S3. The DWS at each velocity model node can be viewed as a proxy for the ray density. Compared to the recovery of the checkerboard tests, $R = 0.6$ is considered a reasonable lower bound for a resolvable area (*36*). *R* is therefore used as an index to shade areas with values smaller than 0.6 as in Fig. 2 and 3.

Estimate of Fresnel zone widths

Following the derivation (*43*) in a 3-D homogenous medium, a simplified calculation of a Fresnel zone width, *f*, is as follows:

$$f = 2\left[\frac{\lambda d(L-d)}{L}\right]^{\frac{1}{2}} \quad \text{(S2)}$$

where λ is the wavelength, *L* is the total distance between source and receiver, and d is the distance from the source or receiver. Given the 1-s period of teleseismic *P*-waves used and the ~6 km/s average crustal V_P, the wavelength of a teleseismic wave is 6 km. Using the *Taup* toolkit (*44*) with the *ak135* global 1-D model (*39*) for a distance range of 30° to 90°, the length of the ray path, *L*, is calculated to be ~3,600 and ~11,350 km for the 30° and 90° epicentral distances of the teleseismic data, respectively. For an example lower-crustal LVB at 20-40 km, assuming d is 30 km from the receiver, we will then have a Fresnel zone width of ~27 km for either the shortest (30°) or the longest (90°) epicentral distances. This calculation shows that the 1-s teleseismic *P*-wave data that we used in the study are able to resolve any structure with a radius larger than ~27 km, for which the imaged lower-crustal LVB is much larger. However, considering the typical dimensions observed at field outcrops, the volcanic dikes inferred to exist between the two crustal LVBs cannot be detected seismically in this case.

Velocity anomalies caused by temperature

Granite and the mafic granulite are widely accepted as the primary composition of the Snake River Plain upper and lower crust, respectively (*5*). As a part of the Snake River Plain bimodal silicic-basaltic volcanic sequence, the crustal composition beneath the Yellowstone caldera is likely similar. From laboratory experiments with a global compilation dataset (*45*), mafic granulite has an average V_P of ~6.8 km/s and a temperature coefficient of -0.52×10^3 km/s/°C. Assuming the mantle plume is the dominant heat source and perfectly transfers the heat into the lowermost crust, we can then use the excess temperature of the plume to assess the velocity reduction in the lower crust. Previous studies have suggested the excess temperature of the Yellowstone plume to be 55-120 K (*2, 46*). Using this value together with the temperature coefficient of mafic granulite gives a V_P decrease of 0.029-0.062 km/s, corresponding to a 0.4-0.9% velocity reduction. Thus, the composition and the temperature variations are not likely to be large enough to explain the high V_P reductions observed in the lower crust and require an additional source, such as partial melts, to account for the observation. For the upper-crustal rhyolitic reservoir, the melt fraction calculation uses a relation that has taken in situ high temperatures into account (*13*).

Volume estimate of crustal magma bodies

Quantifying the uncertainties of tomographic inversions is challenging. In this study, we tend to be conservative and provide a lower-bound estimate, e.g. 5% V_P reduction. We then discretize the model space into 8 km3 cubes and integrate those within a 5% contour of V_P reduction to obtain the total volumes. Note that the bottom of the lower crustal reservoir is fixed at the Moho depth of 45 km (*26*) for calculation because of its relatively poorer resolution (Fig. S6). Different volume estimates using different choices of V_P reduction are shown in Fig. S7. Based on the previous section, temperature anomalies could contribute up to 1% of the V_P reduction. Moreover, thermal considerations suggest that the

volume of basaltic magma parental to the rhyolite will be at least three to five times greater than that of derivative silicic magma (*27*). Because choosing a V_P reduction greater than 6% results in a volume ratio smaller than 3 (Fig. S7C), we therefore narrow the possible range of V_P reduction to 2-6 %. The range then results in volumes of 8,000-18,000 km3 for the upper crustal reservoir and 30,000-116,000 km3 for lower crustal one, respectively. The volume gradient with respect to the V_P reduction also reveals that the boundary of upper crustal reservoir is much sharper than that of the lower crustal reservoir (Figure S7A).

Melt fraction of crustal magma bodies

A relationship between absolute *P*-wave and *S*-wave velocities with respect to various porosities with melt and fluid saturations has been determined by (*13*) based on an assumption of a fluid-saturated porous material consisting of granite and a mixture of rhyolite melt and water and CO_2 at a temperature of 800°C and pressure at 5 km depth (0.1 GPa) for an upper-crust rhyolitic magma body beneath the Yellowstone caldera. Following this relation, we averaged the V_P over the volume of the upper-crustal LVB and get 5.21 km/s. Introducing this value into the relation gives ~9% porosity (i.e., melt fraction). Note that this relation assumes all pore fluids are in the equilibrium state throughout the pore space. Theoretically, we can derive a similar relation for the lower-crustal magma reservoir by replacing rhyolite with basalt and granite with granulite. However, this relation would rely on absolute velocity information, which is inherently lost when demeaned relative travel times of the teleseimic data are used. So for the structures mainly constrained by the teleseismic data, e.g. for depths greater than 20 km based on our tests (Fig. S4, S5, S6), this relation may not be applicable. Thus, a melt-fraction relation with respect to the V_P perturbation for the upper mantle peridotite-basalt-melt system is taken (*47*, *48*), by assuming similar elastic properties between the lower crust and the uppermost mantle beneath the Yellowstone caldera. This assumption is approximate but likely close to reality because of the high velocity and dense underplated layers that have been reported for the Snake River Plain (*5, 33*). According to different partial derivatives with different shapes and states of melt inclusions (Table S2), and given an average V_P reduction of 6.56% calculated over the V_P =-5% contour of the lower-crustal LVB, we estimate a 2-5% melt fraction (Table S2). Because the Yellowstone magmatic system inflates and deflates at rates of ~2-3 cm/yr (*5*), i.e., based on historic GPS measurements, and the extraordinary thermal and CO_2 degassing properties require a contribution from the deep basaltic reservoir (*7, 8*), the relaxed state that represents the pressure equilibrium inclusions with high connectivity and mobility of melts is more preferable in this case. Thus, using the V_P reduction derivatives of 3.6% (Table S2) gives us a ~2% melt fraction and a potential melt volume of 900 km3. Since the existence of water and gas bubbles can also lower the seismic velocity (*13*), these estimates should be regarded as an upper bound for melt fraction.

CO_2 depletion time of crustal magma bodies

We convert the daily CO_2 surface emission rate (45,000 ± 16,000 tons/day) into an annual emission rate of 1.642×1010 kg/yr. Assuming that 50% of the degassed output originates from the subsurface magma, as estimated by carbon and helium isotopes (*28*), the annual emission rate of CO_2 contributed from the magma is 8.21×109 kg/yr. Given the parameters listed in Table S3, the total CO_2 mass dissolved within a magma reservoir can then be calculated as the following:

$$M_{CO_2} = M_{melt} \times r = D_{melt} \times V_{melt} \times r \quad \text{(S3)}$$

where M_{melt} and M_{CO_2} are the mass of the melts and the dissolved CO_2. Replacing M_{melt} with the product of density D_{melt}, and volume V_{melt}, and given the CO_2 abundance, *r*, we obtain estimates of the current dissolved CO_2 mass of 8.4×1011 kg and 2.7×1013 kg for the upper- and lower-crustal LVBs, respectively. The summed CO_2 mass of the two LVBs divided by the annual emission rate of magma-contributed CO_2 then results in a ~3,300 year CO_2 depletion time assuming no replenishment from the mantle source.

The high intensity of the Yellowstone hydrothermal system has been suggested to be active for ~15,000 years or longer (*29*). If we assume the entire magma reservoir is a consequence of the solidification of previous melts, the onset time of CO_2 degassing can then be estimated by replacing the melt volume (e.g. 9%) with the solidified portion of the magma body volume (e.g. 91%) in Eq. S3. Similar calculations have been previously done for the rhyolitic magma reservoir (*6, 13*) and gave ~1000 years, which is far less than the 15,000 years for the age of the hydrothermal system and therefore led to a claim of additional basaltic input (*6, 7, 13*). Introducing the magma body volume obtained in this study, we obtain 1,100 and 160,000 years ago for the CO_2 onset time for the rhyolitic and basaltic reservoirs, respectively. The rhyolite estimate agrees well with those in previous studies, and the basalt estimate gives a time an order of magnitude longer than ~15,000 years, and between the occurrence of the youngest rhyolite flow (70 ka) and the caldera forming eruption (0.64 Ma) (*1*). This implies that the imaged lower crustal basaltic reservoir is sufficient to sustain the overlying rhyolitic reservoir and to supply the large discharge of CO_2, although whether the CO_2 from the basaltic reservoir always goes through the overlying rhyolitic reservoir or in part through some direct path to the surface is unknown. Finally, we point out that the lateral migration of gas and potential ground water level change after the last glaciation termination at ~14,000 years (*29*) are also variables that hinder the calculation from being more detailed.

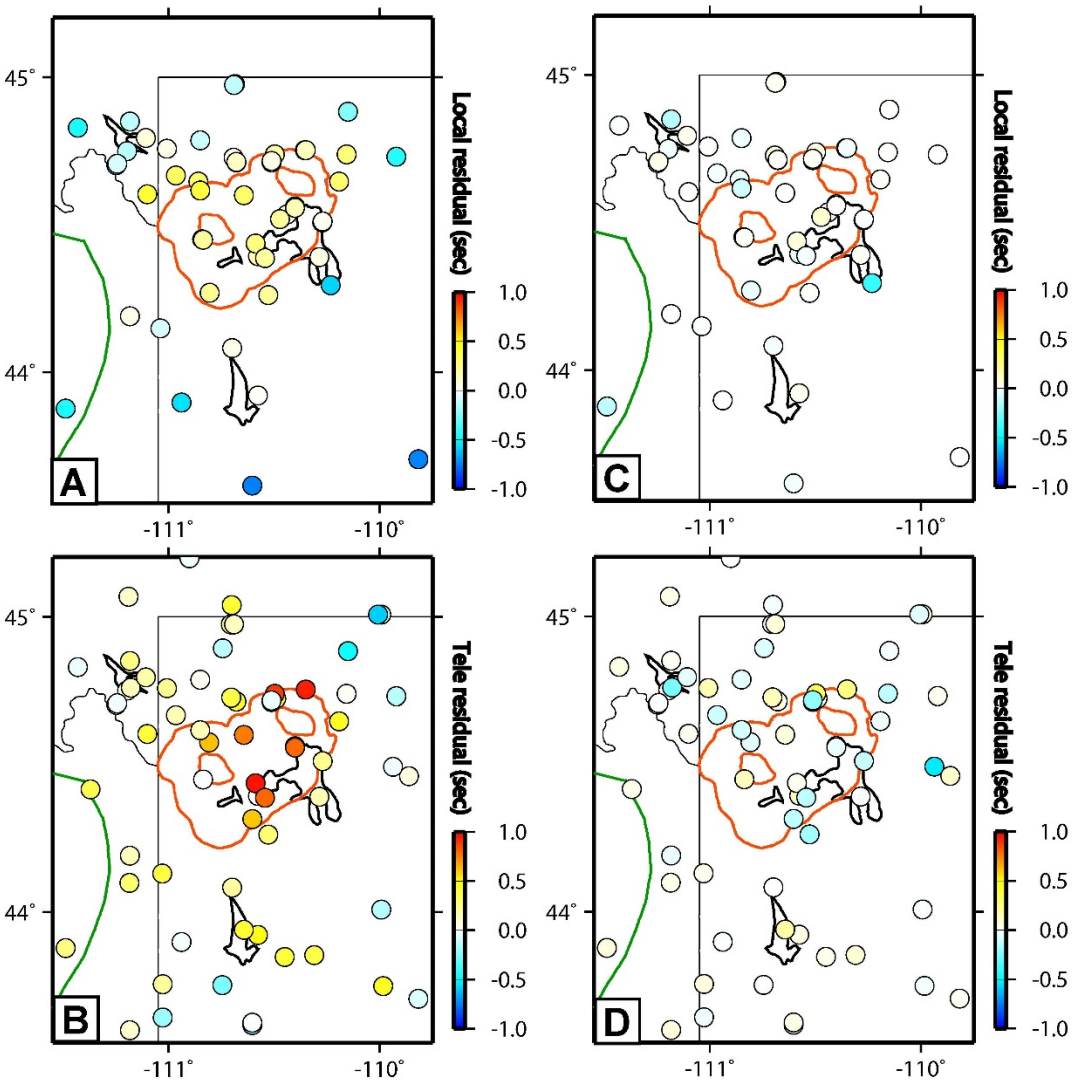

Fig. S1. Averaged seismic station *P*-wave time residual map before and after the joint inversion. Initial residuals of local earthquake arrival times (A) and teleseismic differential times (B) before inversion, and final residuals of local earthquake arrival times (C) and teleseismic differential times (D) after the inversion.

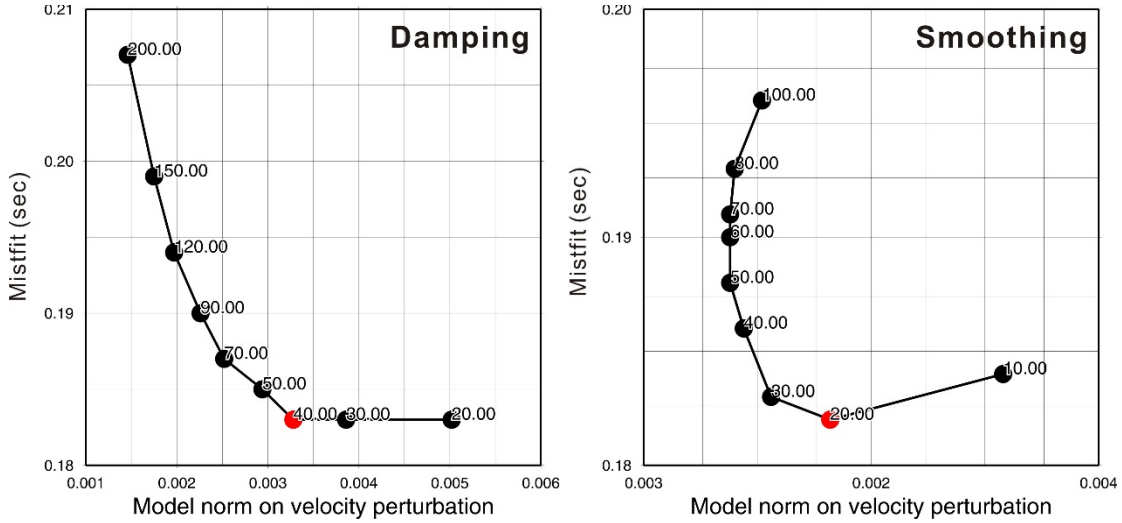

Fig. S2 Trade-off curve tests for damping and smoothing parameters. The labeled black dots are different damping and smoothing values we tested, and the labeled red dots are the final choices used for the inversion.

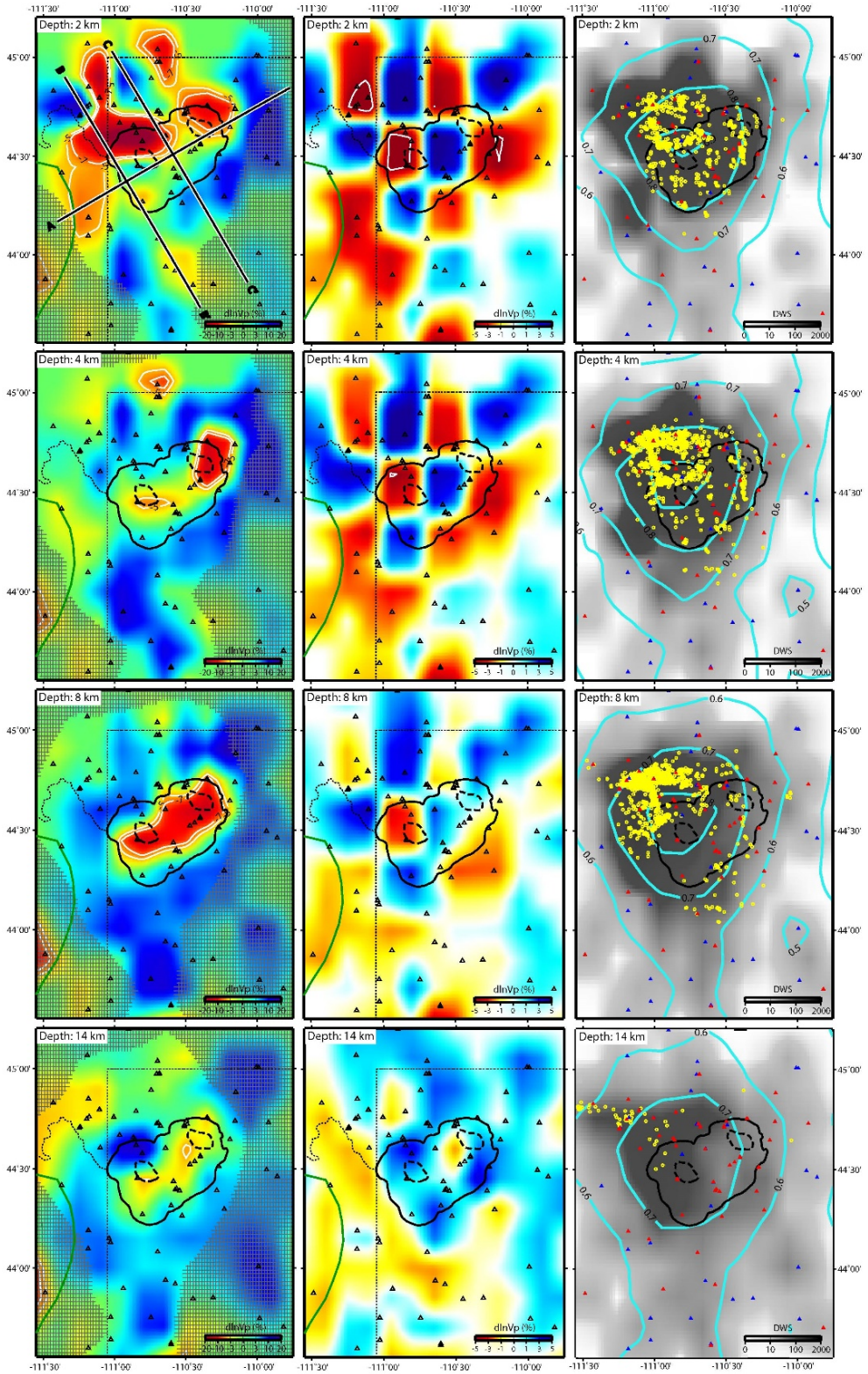

Fig. S3 Inverted *P*-wave velocity model, checkerboard test, and derivative weighted sum (DWS) at each depth.

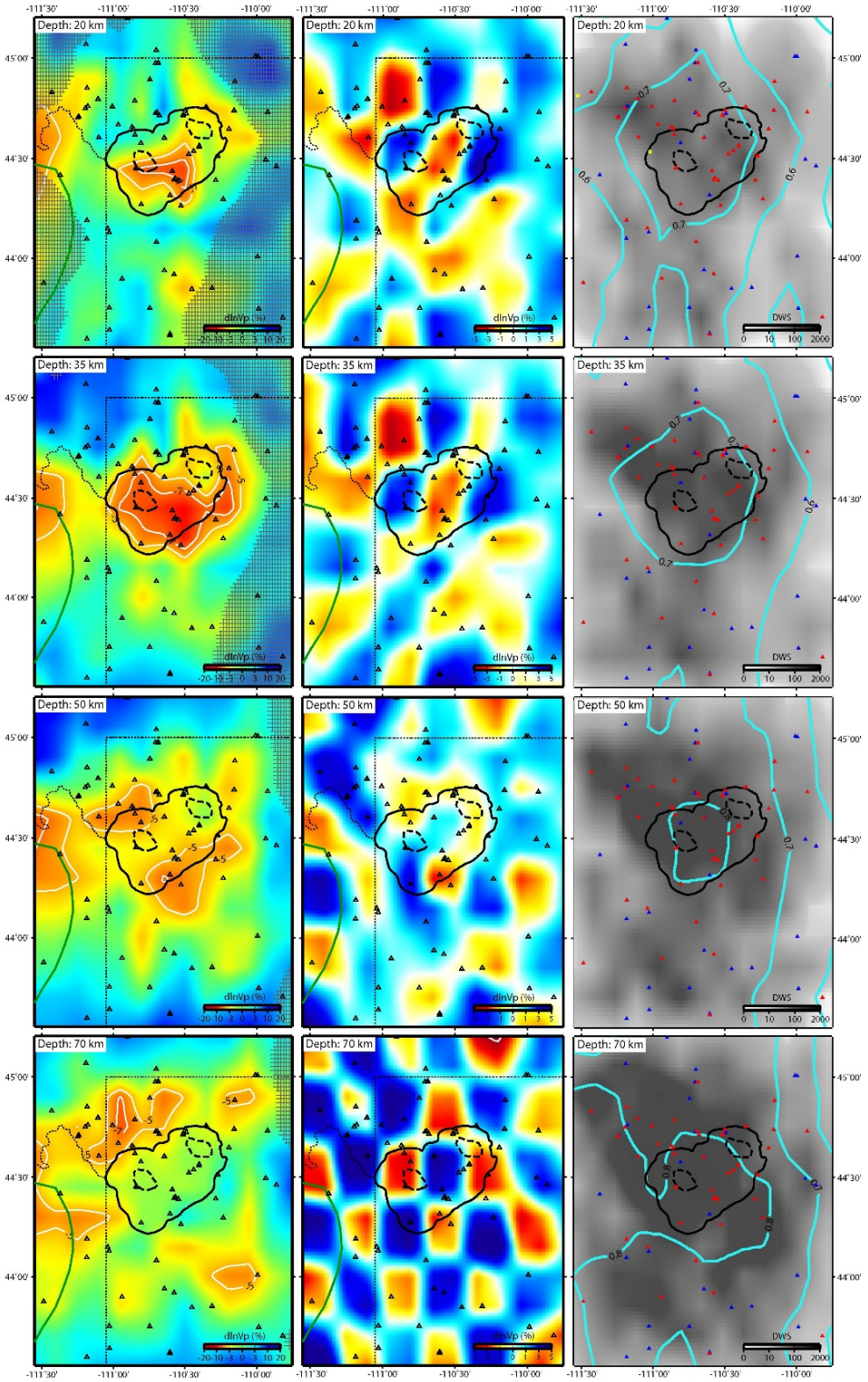

Fig. S3 Inverted *P*-wave velocity model, checkerboard test, and derivative weighted sum (DWS) at each depth (continued).

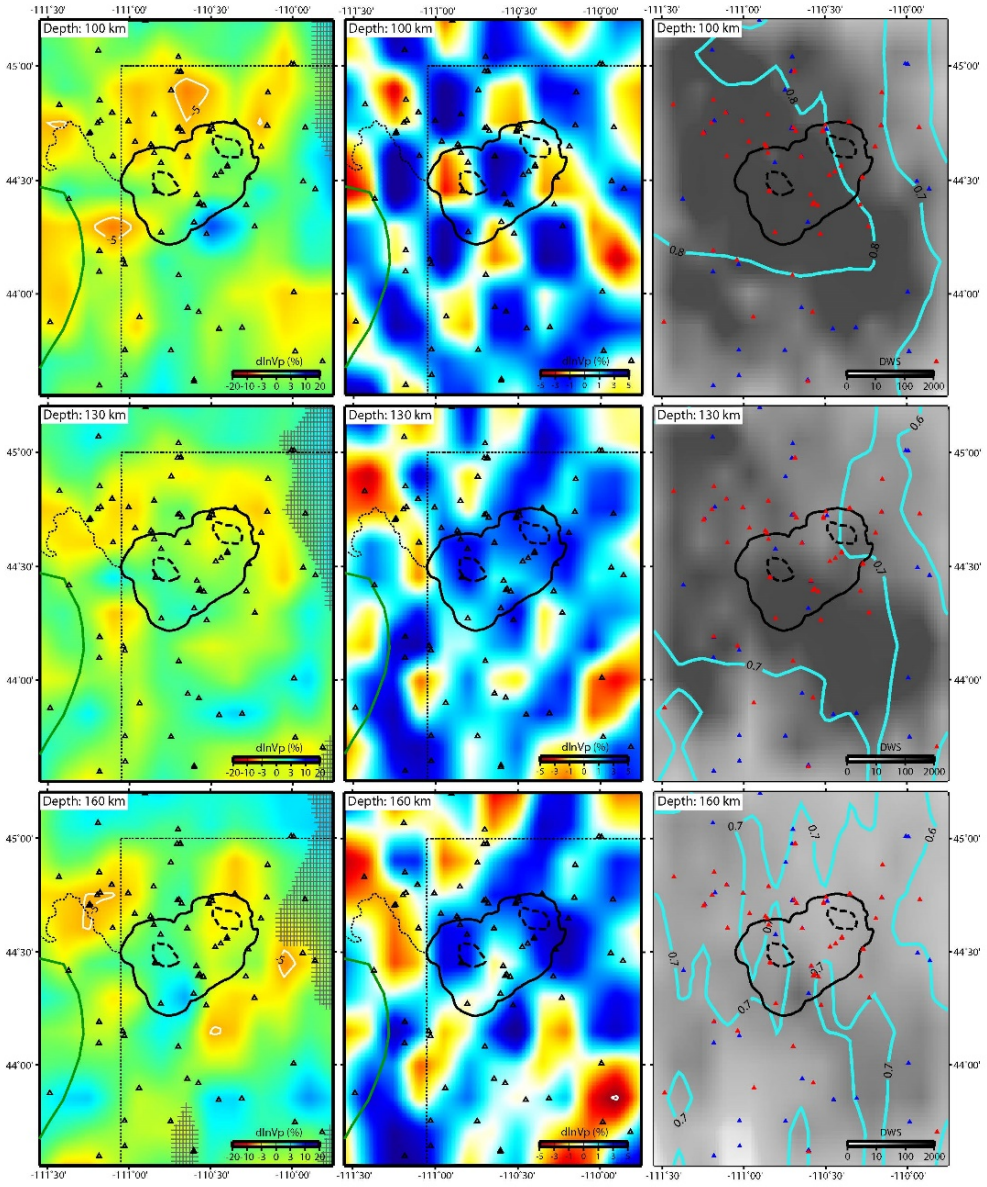

Fig. S3 Inverted *P*-wave velocity model, checkerboard test, and derivative weighted sum (DWS) at each depth (continued). Black thick solid, dashed, and thin dotted lines denote the Yellowstone caldera, resurgent domes in the caldera, and the state borders, respectively. Green lines represent the tectonic division of the Eastern Snake River Plain. The locations of cross-sections are shown on the depth slice of 2 km. Stations are indicated as black triangles in the left and middle columns. On the right column, red and blue triangles represent the stations that record and do not record the local earthquakes, respectively. Note that teleseismic earthquakes are recorded by both the red and blue stations. Yellow circles and cyan contours show the local earthquake distribution and the translated resolvability, *R*, from Eq. S1 at different depths.

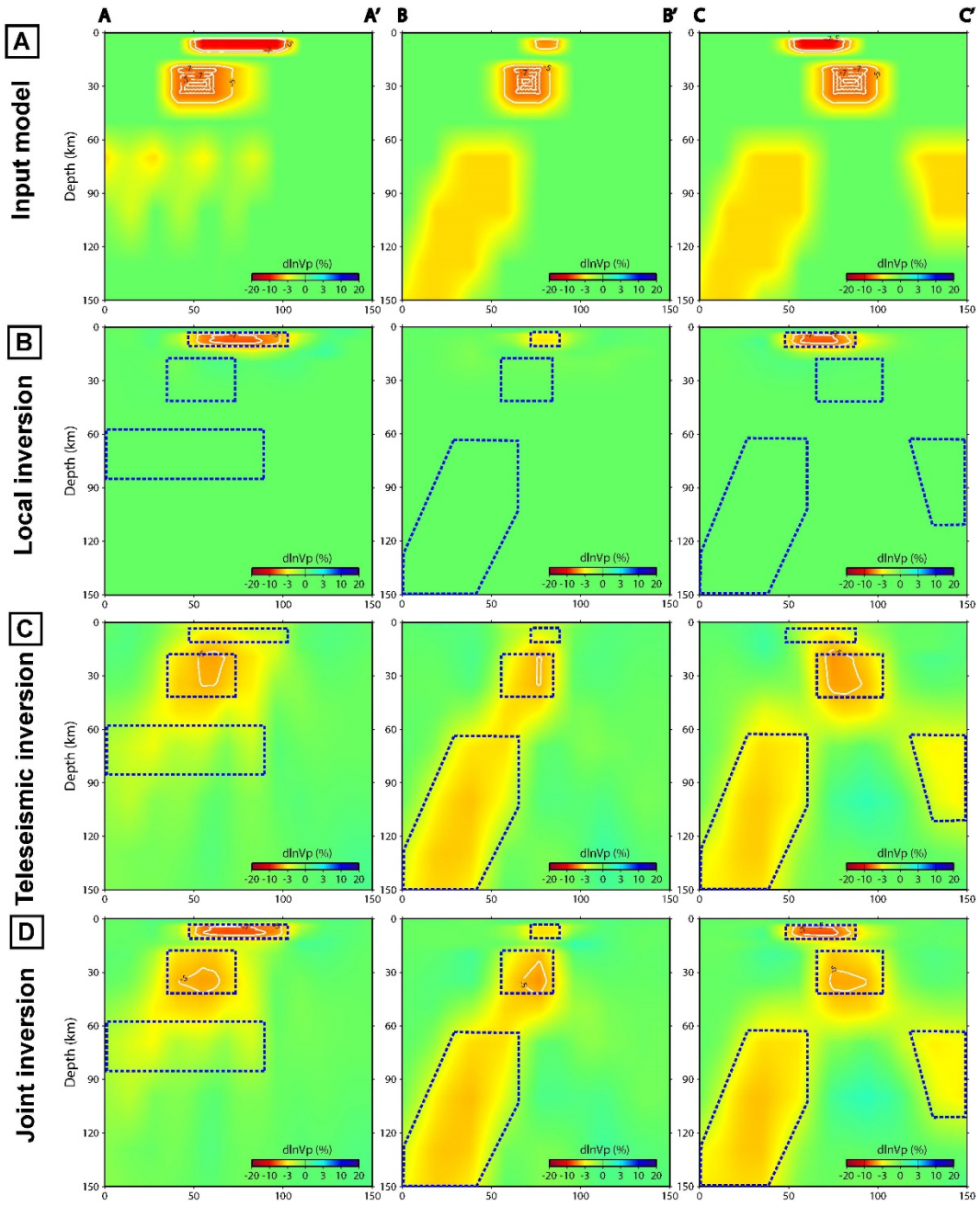

Fig. S4 Characteristic model test for local earthquake, teleseismic, and joint inversions. The input model (A) and the recovered images from the inversion with local data alone (B), with teleseismic data alone (C), and jointly with local and teleseismic data together (D). Blue dotted lines denote the approximate boundaries of input LVAs.

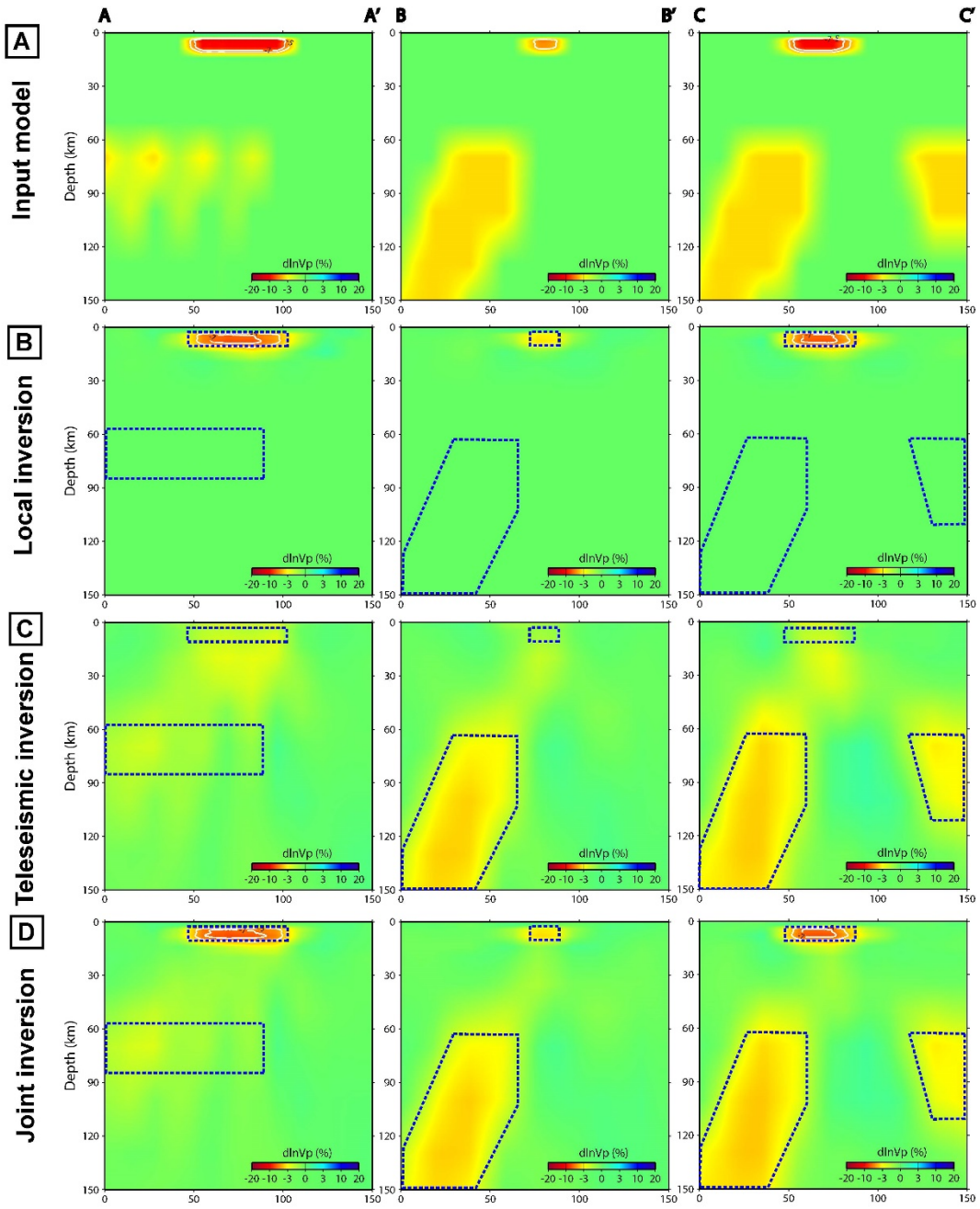

Fig. S5 Characteristic model test without the lower-crustal anomaly for local earthquake, teleseismic, and joint inversions. The input model (A) and the recovered images from the inversion with local data alone (B), with teleseismic data alone (C), and jointly with local and teleseismic data together (D). Blue dotted lines denote the approximate boundaries of input LVAs.

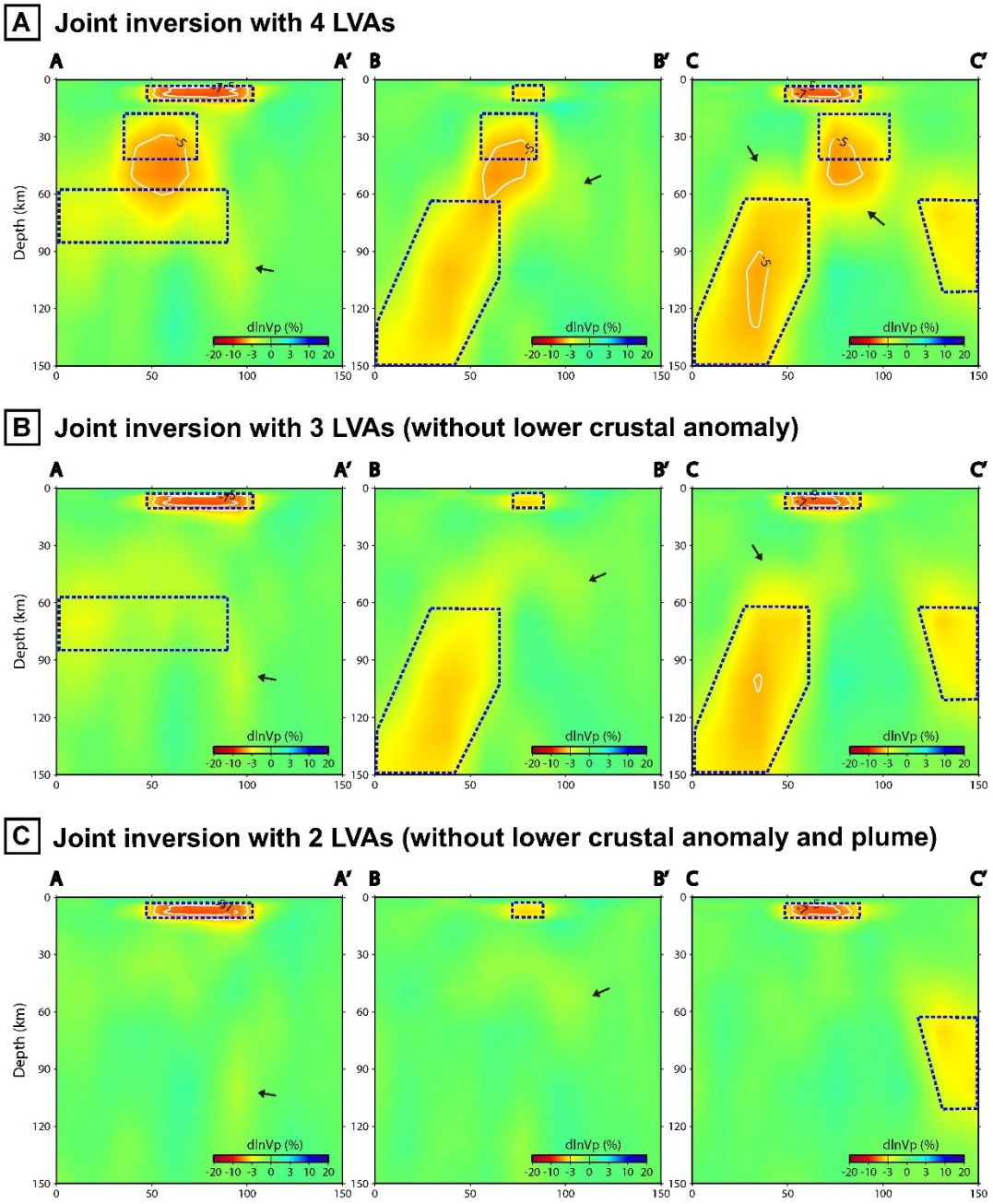

Fig. S6 Characteristic model test with noise level of 0.13 s. Testing the smearing with noise for a model with (A) 4 LVAs, (B) with 3 LVAs (without lower crustal anomaly), and (C) with 2 LVAs (without lower crustal anomaly and plume). All results are by joint inversion of local earthquake and teleseismic data. Blue dotted lines denote the approximate boundaries of input LVAs shown in Fig. S4A. Black arrows indicate the smearing artifacts.

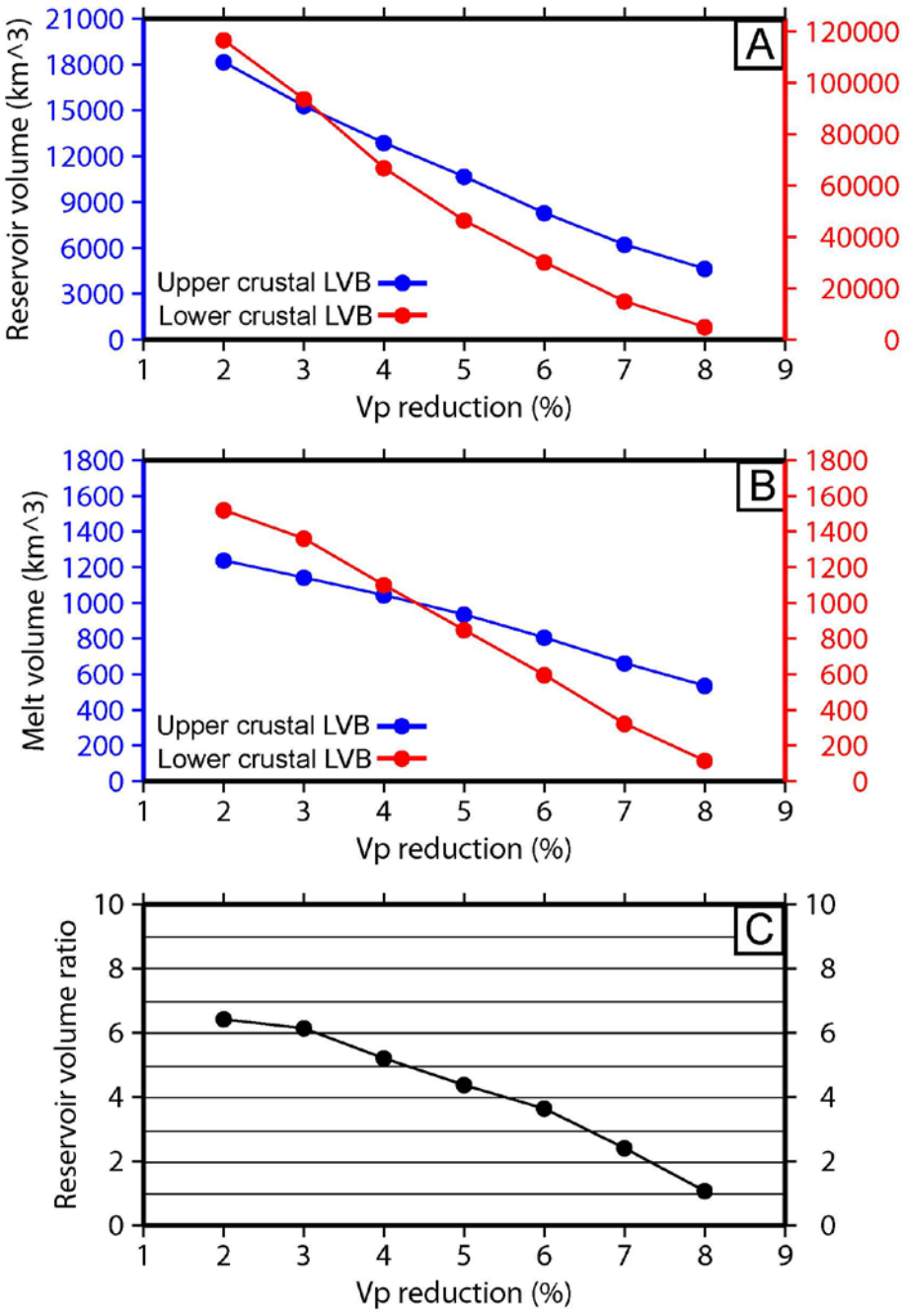

Fig. S7 Volume estimate and ratio with different V_P reduction (%). (A) Estimates of magma reservoir volume; (B) Estimates of partial melt volume; and (C) Ratio between upper and lower crustal magma reservoir volume.

Table S1. Initial 1-D *P*-wave velocity model used in this study.

Model nodes at depth (km)	***P*-wave velocity (km/s)**
-10.0	3.700
-4.0	3.800
2.0	5.240
4.0	5.420
8.0	5.650
14.0	6.120
20.0	6.300
35.0	6.500
50.0	7.500
70.0	8.015
100.0	8.048
130.0	8.080
160.0	8.156

Table S2. Reference partial derivatives of *P*-wave velocity with respect to melt fraction. Velocity reduction derivatives are in percentage. The unrelaxed state and the relaxed state represent the conditions of isolated inclusions and pressure-equalized inclusions. V_P, *P*-wave velocity (km/s); F, melt fraction (%). Numbers in parentheses denote references.

$-\partial \ln V_P / \mathrm{dF}$	Melt inclusion description
1.23	Unrelaxed state, dihedral angle typical (*48*)
2.9	Unrelaxed state, organized cuspate shape (*47*)
3.6	Relaxed state, organized cuspate shape (*47*)

Table S3. Geophysical and geochemical parameters used for the CO_2 calculation. Numbers in parentheses denote references.

Magma type	Density (kg/km^3)	CO_2 abundance in the melts (ppm)	Reservoir volume (km^3)	Melt volume (km^3)
Basalt	2.9×10^{12} (*28*)	10,000 (6)	46,000 (*)	900 (*)
Rhyolite	2.2×10^{12} (*13*)	400 (6)	10,000 (*)	900 (*)

* derived from this study.

References

1. R. L. Christiansen, *U.S. Geol. Surv. Prof. Pap. 729-G*, 145 (2001).

2. R. B. Smith, M. Jordan, B. Steinberger, C. M. Puskas, J. Farrell, G. P. Waite, S. Husen, W. L. Chang, R. O'Connell, Geodynamics of the Yellowstone hotspot and mantle plume: Seismic and GPS imaging, kinematics, and mantle flow. *J. Volcanol. Geotherm. Res.* **188**, 26–56 (2009). doi:10.1016/j.jvolgeores.2009.08.020

3. J. Farrell, R. B. Smith, S. Husen, T. Diehl, Tomography from 26 years of seismicity revealing that the spatial extent of the Yellowstone crustal magma reservoir extends well beyond the Yellowstone caldera. *Geophys. Res. Lett.* **41**, 3068–3073 (2014). doi:10.1002/2014GL059588

4. W. L. Chang, R. B. Smith, C. Wicks, J. M. Farrell, C. M. Puskas, Accelerated uplift and magmatic intrusion of the Yellowstone caldera, 2004 to 2006. *Science* **318**, 952–956 (2007). Medline doi:10.1126/science.1146842

5. K. R. DeNosaquo, R. B. Smith, A. R. Lowry, Density and lithospheric strength models of the Yellowstone–Snake River Plain volcanic system from gravity and heat flow data. *J. Volcanol. Geotherm. Res.* **188**, 108–127 (2009). doi:10.1016/j.jvolgeores.2009.08.006

6. J. B. Lowenstern, S. Hurwitz, Monitoring a supervolcano in repose: Heat and volatile flux at the Yellowstone caldera. *Elements* **4**, 35–40 (2008). doi:10.2113/GSELEMENTS.4.1.35

7. S. Hurwitz, J. B. Lowenstern, Dynamics of the Yellowstone hydrothermal system. *Rev. Geophys.* **52**, 375–411 (2014). doi:10.1002/2014RG000452

8. H. Yuan, K. Dueker, Teleseismic *P*-wave tomogram of the Yellowstone plume. *Geophys. Res. Lett.* **32**, L07304 (2005). doi:10.1029/2004GL022056

9. M. Xue, R. M. Allen, Mantle structure beneath the western United States and its implications for convection processes. *J. Geophys. Res.* **115**, B07303 (2010). doi:10.1029/2008JB006079

10. M. Obrebski, R. M. Allen, F. Pollitz, S. H. Hung, Lithosphere-asthenosphere interaction beneath the western United States from the joint inversion of body-wave traveltimes and surface-wave phase velocities. *Geophys. J. Int.* **185**, 1003–1021 (2011). doi:10.1111/j.1365-246X.2011.04990.x

11. B. Schmandt, K. Dueker, E. Humphreys, S. Hansen, Hot mantle upwelling across the 660 beneath Yellowstone. *Earth Planet. Sci. Lett.* **331–332**, 224–236 (2012). doi:10.1016/j.epsl.2012.03.025

12. S. Husen, R. B. Smith, G. P. Waite, Evidence for gas and magmatic sources beneath the Yellowstone volcanic field from seismic tomographic imaging. *J. Volcanol. Geotherm. Res.* **131**, 397–410 (2004). doi:10.1016/S0377-0273(03)00416-5

13. R. Chu, D. V. Helmberger, D. Sun, J. M. Jackson, L. Zhu, Mushy magma beneath Yellowstone. *Geophys. Res. Lett.* **37**, L01306 (2010). doi:10.1029/2009GL041656

14. M. Paulatto, C. Annen, T. J. Henstock, E. Kiddle, T. A. Minshull, R. S. J. Sparks, B. Voight, Magma chamber properties from integrated seismic tomography and thermal modeling at Montserrat. *Geochem. Geophys. Geosyst.* **13**, Q01014 (2012). doi:10.1029/2011GC003892

15. M. A. Mitchell, R. S. White, S. Roecker, T. Greenfield, Tomographic image of melt storage beneath Askja Volcano, Iceland using local microseismicity. *Geophys. Res. Lett.* **40**, 5040–5046 (2013). doi:10.1002/grl.50899

16. M. West, W. Menke, M. Tolstoy, S. Webb, R. Sohn, Magma storage beneath Axial volcano on the Juan de Fuca mid-ocean ridge. *Nature* **413**, 833–836 (2001). Medline doi:10.1038/35101581

17. E. M. Syracuse, C. H. Thurber, C. J. Wolfe, P. G. Okubo, J. H. Foster, B. A. Brooks, High-resolution locations of triggered earthquakes and tomographic imaging of Kilauea Volcano's south flank. *J. Geophys. Res.* **115**, B10310 (2010). doi:10.1029/2010JB007554

18. G. P. Waite, S. C. Moran, VP Structure of Mount St. Helens, Washington, USA, imaged with local earthquake tomography. *J. Volcanol. Geotherm. Res.* **182**, 113–122 (2009). doi:10.1016/j.jvolgeores.2009.02.009

19. I. Koulakov, E. I. Gordeev, N. L. Dobretsov, V. A. Vernikovsky, S. Senyukov, A. Jakovlev, K. Jaxybulatov, Rapid changes in magma storage beneath the Klyuchevskoy group of volcanoes inferred from time-dependent seismic tomography. *J. Volcanol. Geotherm. Res.* **263**, 75–91 (2013). doi:10.1016/j.jvolgeores.2012.10.014

20. K. J. Seats, J. F. Lawrence, The seismic structure beneath the Yellowstone Volcano Field from ambient seismic noise. *Geophys. Res. Lett.* **41**, 8277–8282 (2014). doi:10.1002/2014GL061913

21. S. W. Roecker, T. M. Sabitova, L. P. Vinnik, Y. A. Burmakov, M. I. Golvanov, R. Mamatkanova, L. Munirova, Three-dimensional elastic wave velocity structure of the western and central Tien Shan. *J. Geophys. Res.* **98**, 15779 (1993). doi:10.1029/93JB01560

22. D. Zhao, A. Hasegawa, H. Kanamori, Deep structure of Japan subduction zone as derived from local, regional, and teleseismic events. *J. Geophys. Res.* **99**, 22313–22329 (1994). doi:10.1029/94JB01149

23. H.-H. Huang, Y.-M. Wu, X. Song, C.-H. Chang, H. Kuo-Chen, S.-J. Lee, Investigating the lithospheric velocity structures beneath the Taiwan region by nonlinear joint inversion of local and teleseismic *P* wave data: Slab continuity and deflection. *Geophys. Res. Lett.* **41**, (2014). doi:10.1002/2014GL061115

24. B. Schmandt, F. C. Lin, *P* and *S* wave tomography of the mantle beneath the United States. *Geophys. Res. Lett.* **41**, 6342–6349 (2014). doi:10.1002/2014GL061231

25. See supplementary materials on *Science* Online.

26. W. Shen, M. H. Ritzwoller, V. Schulte-Pelkum, A 3-D model of the crust and uppermost mantle beneath the Central and Western US by joint inversion of receiver functions and surface wave dispersion. *J. Geophys. Res.* **118**, 262–276 (2013). doi:10.1029/2012JB009602

27. S. M. White, J. A. Crisp, F. J. Spera, Long-term volumetric eruption rates and magma budgets. *Geochem. Geophys. Geosyst.* **7**, Q03010 (2006). doi:10.1029/2005GC001002

28. C. Werner, S. Brantley, CO_2 emissions from the Yellowstone volcanic system. *Geochem. Geophys. Geosyst.* **4**, 1061 (2003). doi:10.1029/2002GC000473

29. R. O. Fournier, Geochemistry and dynamics of the Yellowstone National Park hydrothermal system. *Annu. Rev. Earth Planet. Sci.* **17**, 13–53 (1989). doi:10.1146/annurev.ea.17.050189.000305

30. K. Jaxybulatov, N. M. Shapiro, I. Koulakov, A. Mordret, M. Landès, C. Sens-Schönfelder, A large magmatic sill complex beneath the Toba caldera. *Science* **346**, 617–619 (2014). Medline doi:10.1126/science.1258582

31. C. Annen, J. D. Blundy, R. S. J. Sparks, The genesis of intermediate and silicic magmas in deep crustal hot zones. *J. Petrol.* **47**, 505–539 (2006). doi:10.1093/petrology/egi084

32. A. Gudmundsson, Deflection of dykes into sills at discontinuities and magma-chamber formation. *Tectonophysics* **500**, 50–64 (2011). doi:10.1016/j.tecto.2009.10.015

33. J. W. Shervais, S. K. Vetter, B. B. Hanan, Layered mafic sill complex beneath the eastern Snake River Plain: Evidence from cyclic geochemical variations in basalt. *Geology* **34**, 365 (2006). doi:10.1130/G22226.1

34. Z. J. Xu, X. Song, Joint inversion for crustal and Pn velocities and Moho depth in Eastern Margin of the Tibetan Plateau. *Tectonophysics* **491**, 185–193 (2010). doi:10.1016/j.tecto.2009.11.022

35. H.-H. Huang, Z. Xu, Y.-M. Wu, X. Song, B.-S. Huang, N. L. Minh, First local seismic tomography for Red River shear zone, northern Vietnam: Stepwise inversion employing crustal P and Pn waves. *Tectonophysics* **584**, 230–239 (2013). doi:10.1016/j.tecto.2012.03.030

36. H. H. Huang, Y. M. Wu, X. Song, C. H. Chang, S. J. Lee, T. M. Chang, H. H. Hsieh, Joint V_p and V_s tomography of Taiwan: Implications for subduction-collision orogeny. *Earth Planet. Sci. Lett.* **392**, 177–191 (2014). doi:10.1016/j.epsl.2014.02.026

37. J. Um, C. Thurber, A fast algorithm for two-point seismic ray tracing. *Bull. Seismol. Soc. Am.* **77**, 972–986 (1987).

38. K. Koketsu, S. Sekine, Pseudo-bending method for three-dimensional seismic ray tracing in a spherical Earth with discontinuities. *Geophys. J. Int.* **132**, 339–346 (1998). doi:10.1046/j.1365-246x.1998.00427.x

39. B. L. N. Kennett, E. R. Engdahl, R. Buland, Constraints on seismic velocities in the Earth from traveltimes. *Geophys. J. Int.* **122**, 108–124 (1995). doi:10.1111/j.1365-246X.1995.tb03540.x

40. J. A. Snoke, J. C. Lahr, Locating earthquakes: At what distance can the Earth no longer be treated as flat? *Seismol. Res. Lett.* **72**, 538–541 (2001). doi:10.1785/gssrl.72.5.538

41. C. A. Zelt, Lateral velocity resolution from three-dimensional seismic refraction data. *Geophys. J. Int.* **135**, 1101–1112 (1998). doi:10.1046/j.1365-246X.1998.00695.x

42. C. H. Thurber, D. Eberhart-Phillips, Local earthquake tomography with flexible gridding. *Comput. Geosci.* **25**, 809–818 (1999). doi:10.1016/S0098-3004(99)00007-2

43. J. Spetzler, R. Snieder, The Fresnel volume and transmitted waves. *Geophysics* **69**, 653–663 (2004). doi:10.1190/1.1759451

44. H. P. Crotwell, T. J. Owens, J. Ritsema, The TauP toolkit: Flexible seismic travel-time and ray-path utilities. *Seismol. Res. Lett.* **70**, 154–160 (1999). doi:10.1785/gssrl.70.2.154

45. N. I. Christensen, W. D. Mooney, Seismic velocity structure and composition of the continental crust: A global view. *J. Geophys. Res.* **100**, 9761–9788 (1995). doi:10.1029/95JB00259

46. D. L. Schutt, K. Dueker, Temperature of the plume layer beneath the Yellowstone hotspot. *Geology* **36**, 623 (2008). doi:10.1130/G24809A.1

47. W. C. Hammond, E. D. Humphreys, Upper mantle seismic wave velocity: Effects of realistic partial melt geometries. *J. Geophys. Res.* **105**, 10975 (2000). doi:10.1029/2000JB900041

48. A. Kreutzmann, H. Schmeling, A. Junge, T. Ruedas, G. Marquart, I. Th. Bjarnason, Temperature and melting of a ridge-centred plume with application to Iceland. Part II: Predictions for electromagnetic and seismic observables. *Geophys. J. Int.* **159**, 1097–1111 (2004). doi:10.1111/j.1365-246X.2004.02397.x